Acetonitrile-driven structural change of Li_3InCl_6 enables amorphization of PEO-LiTFSI for enhanced room-temperature performance

Weiye Ma[1], Lun Zhang[2], Guanghan Zhu[2], Hongrui Kang[3], Haiyang Yuan[4], Yongyi Long[5], Zhiyi Pan[1], Zhiqiang Liu[1], Xiaojing Liu[1], Jin Liang[1], Yuxin Liang[1], Zhenduo Cui[1], Shengli Zhu[1], Ying Zhao[5,], Zhonghui Gao[1,]**

[1]School of Materials Science and Engineering, Tianjin University, Tianjin 300350, China.

[2]Department of Chemical Engineering, University College London, Roberts Building, Torrington Place, London WC1E 7JE, UK.

[3]Technische Universität Darmstadt, Materials Science Department, Surface Science Division Jovanka-Bontschits-Str. 2, 64287 Darmstadt, Germany.

[4]School of Materials Science and Engineering, East China University of Science and Technology, Shanghai 200237, China.

[5]School of Aerospace Engineering and Applied Mechanics, Tongji University, Shanghai 200092, China.

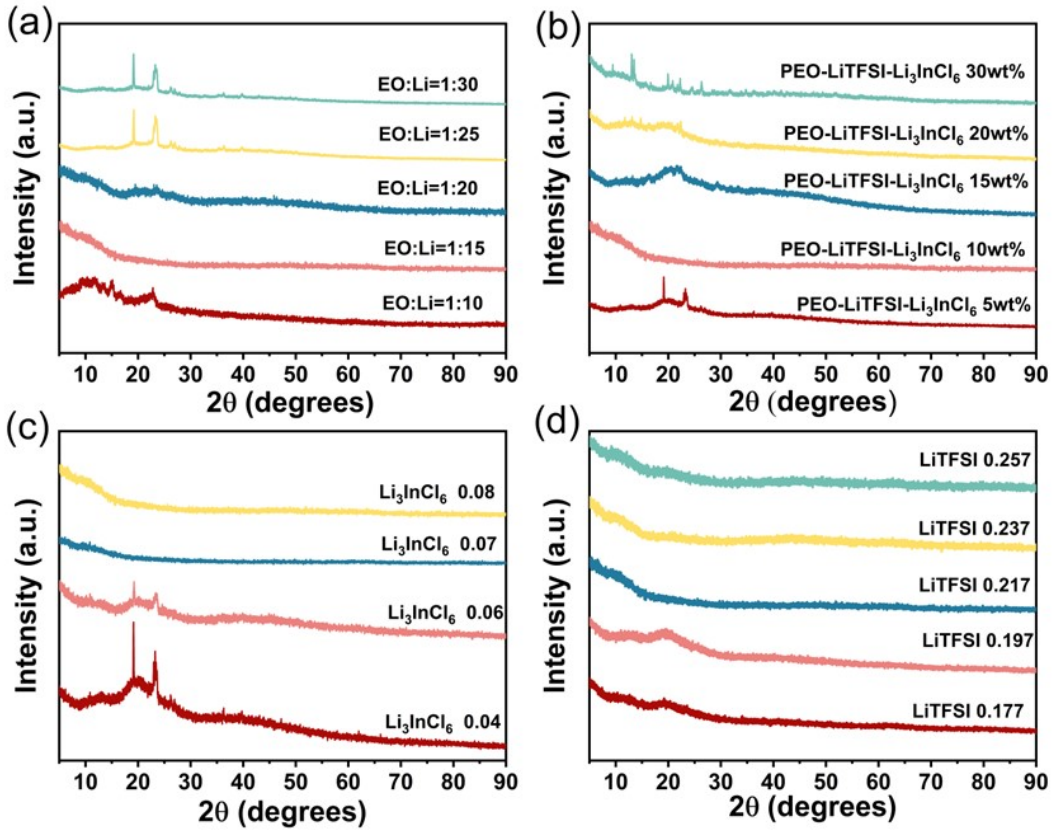

Figure S1. XRD patterns of composite polymer electrolytes (CPEs) with (a) different EO:Li molar ratios and (b) varying mass ratios of Li_3InCl_6. Based on the optimal ratio (PEO-LiTFSI-Li_3InCl_6 10 wt.%) of PEO (0.5 g), LiTFSI (0.217 g), and Li_3InCl_6 (0.08 g), fine-tuning of the mass of (c) Li_3InCl_6 and (d) LiTFSI are presented.

X-ray diffraction (XRD) analysis was conducted on PEO–LiTFSI samples with different Li_3InCl_6 contents to evaluate its influence on the crystallinity, as shown in Figure S1. At a constant amount of LiTFSI, PEO was found to undergo increased amorphization with the progressive addition of Li_3InCl_6. At a Li_3InCl_6 loading of 10 wt.%, PEO was rendered fully amorphous and no residual Li_3InCl_6 was detected. In contrast, when the loading increased to 30 wt.%, partial recrystallization of PEO and the emergence of crystalline Li_3InCl_6 were observed, primarily due to the incomplete intercalation activation of Li_3InCl_6 by acetonitrile, which reduced its plasticizing function to disrupt the PEO crystalline structure. Furthermore, when the Li_3InCl_6 loading exceeds 30 wt.%, the homogeneity of the slurry is significantly reduced, leading to an increased tendency for the different phases separation.

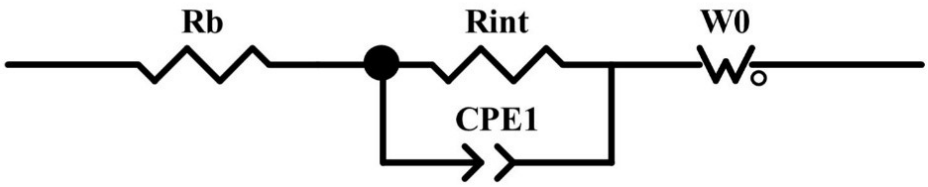

Figure S2. Equivalent circuit used for fitting the EIS spectra of the Li/CPE/Li symmetric cell, where R_b represents bulk resistance and R_{int} represents interfacial resistance.

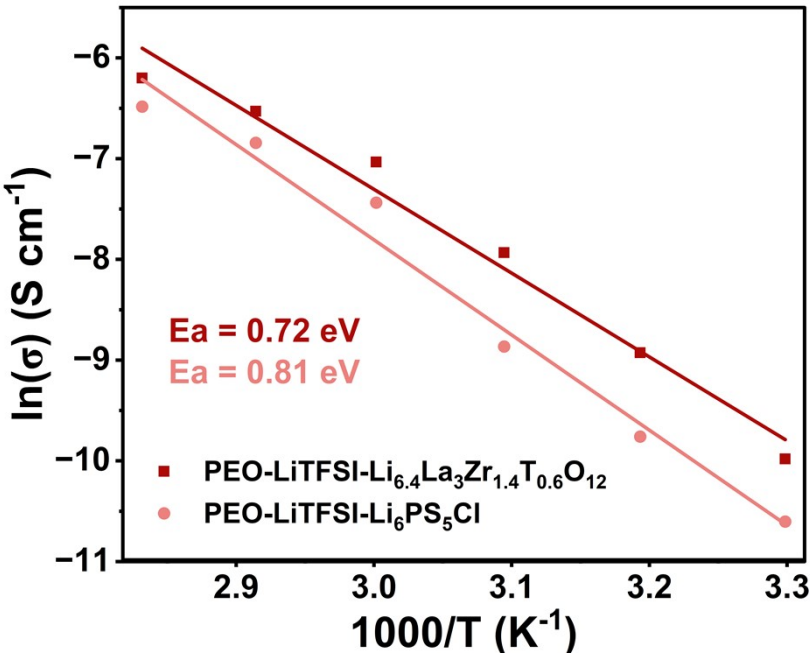

Figure S3. Temperature-dependent ionic conductivities of PEO–LiTFSI–$Li_{6.4}La_3Zr_{1.4}Ta_{0.6}O_{12}$ and PEO–LiTFSI–Li_6PS_5Cl CPEs.

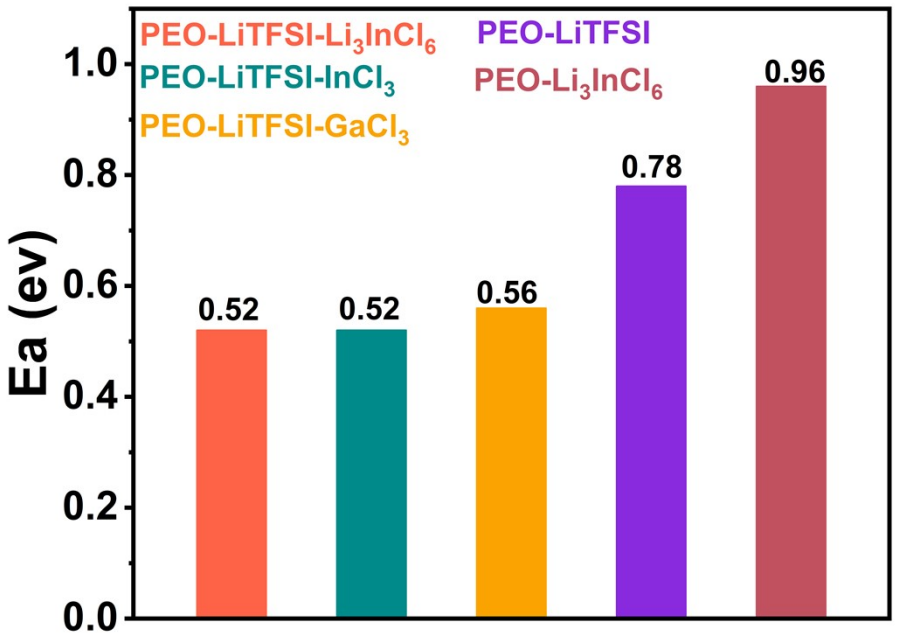

Figure S4. Activation energy(Ea) for Li^+ transport corresponding to different electrolytes

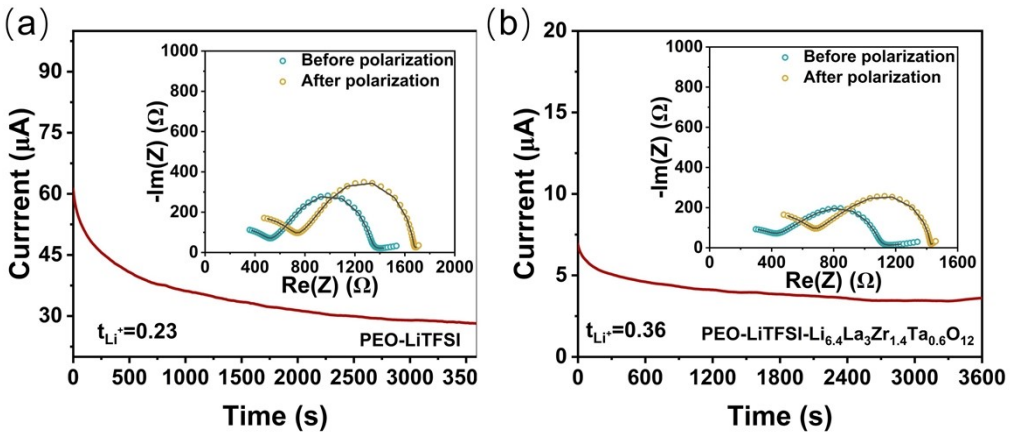

Figure S5. Results of time dependence of potentiostatic polarization current for (a) Li/PEO-LiTFSI/Li and (b) Li/PEO-LiTFSI-$Li_{6.4}La_3Zr_{1.4}Ta_{0.6}O_{12}$/Li symmetric cells and the EIS before and after polarization (inset).

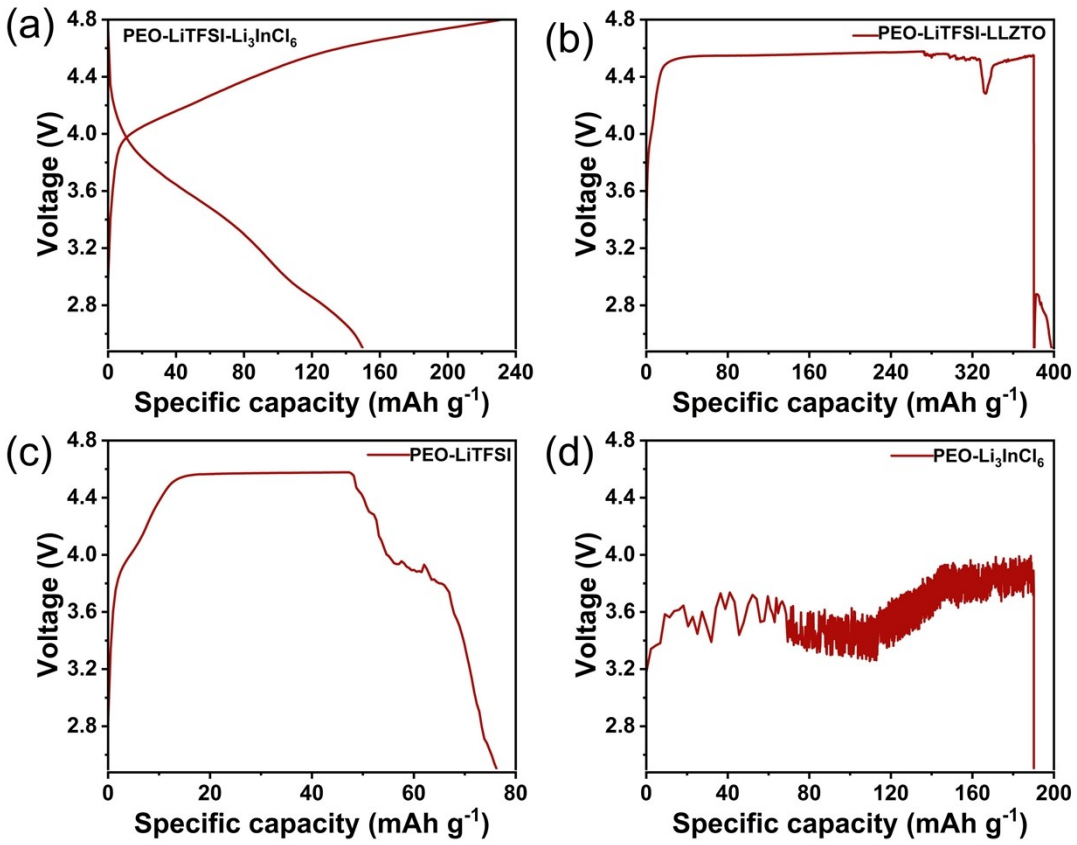

Figure S6. Charge–discharge voltage profiles of high voltage Li-metal batteries with $Li_{1.2}Mn_{0.54}Ni_{0.13}Co_{0.13}O_2$ cathodes paired with (a) PEO–LiTFSI-Li_3InCl_6, (b) PEO–LiTFSI–$Li_{6.4}La_3Zr_{1.4}Ta_{0.6}O_{12}$, (c) PEO–LiTFSI, and (d) PEO–Li_3InCl_6 electrolytes, using Li metal anodes at room temperature. Cells were charged to 4.8 V vs. Li/Li^+.

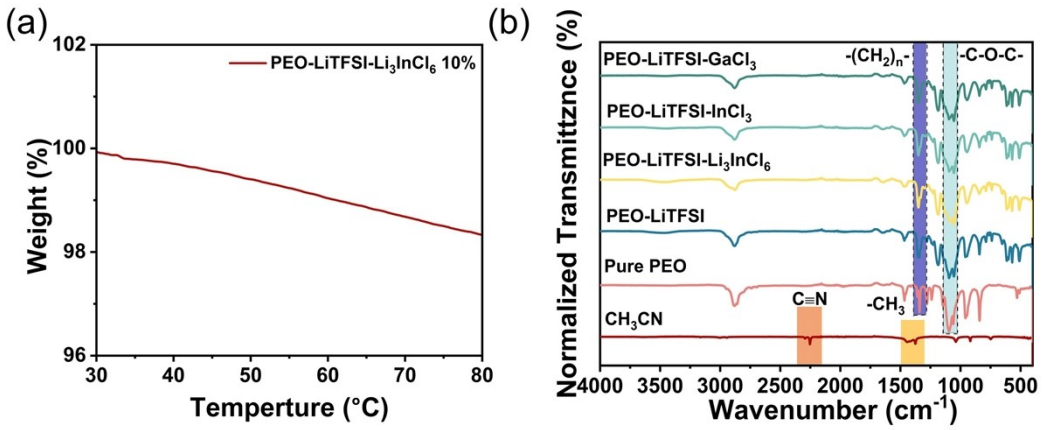

Figure S7. (a) Thermogravimetric analysis (TGA) curves of PEO-LiTFSI-Li_3InCl_6 electrolytes. (b) FTIR spectra of PEO, PEO–LiTFSI, and composite electrolytes with various halide additives, confirming that acetonitrile solvent has completely evaporated.

Given the significant impact of residual solvent on ionic conductivity, a comprehensive characterization including TGA and FTIR were performed to investigate the residual acetonitrile solvent in the PEO-LiTFSI-Li_3InCl_6 CPE. As shown in Figure S7a, Thermogravimetric analysis shows that the PEO-LiTFSI-Li_3InCl_6 CPE sample undergoes only ~1.3% weight loss from 30 °C to 80 °C. That is mainly due to the strong hygroscopic nature of Li_3InCl_6 during the synthesis and transfer processes. FTIR spectra (Figure S7b) reveal no characteristic absorption bands attributable to the C≡N functional group of acetonitrile, indicating the absence of residual solvent in PEO-LiTFSI based CPEs with different amounts of Li_3InCl_6 active filler.

Figure S8. Digital photos of the CPE's thickness measurement by using micrometer. The thickness of the PEO-LiTFSI-Li_3InCl_6 CPE sample is 225 μm.

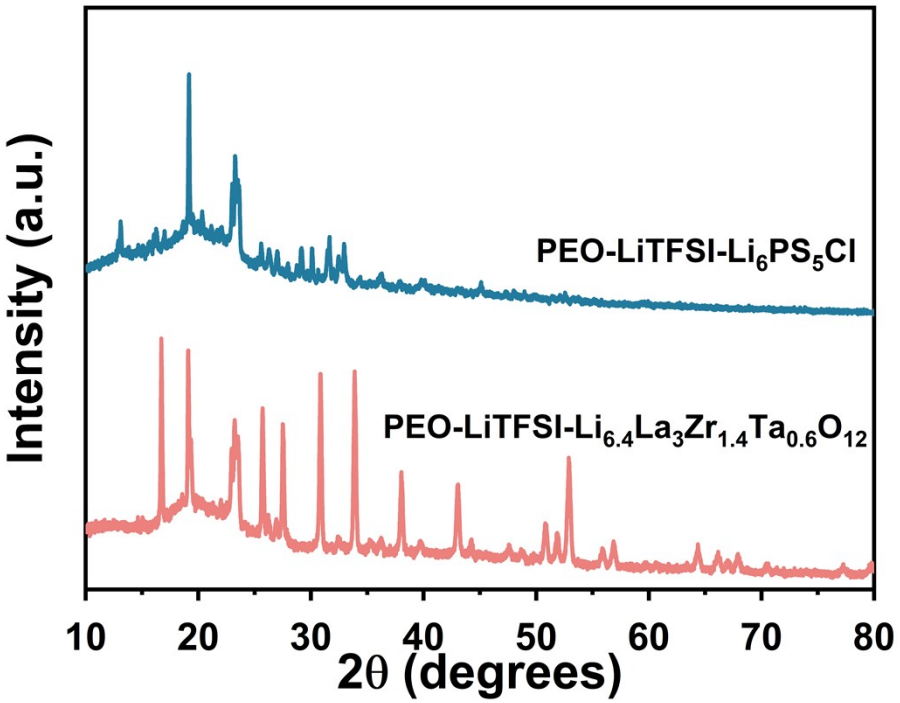

Figure S9. XRD patterns of composite polymer electrolytes (CPEs)

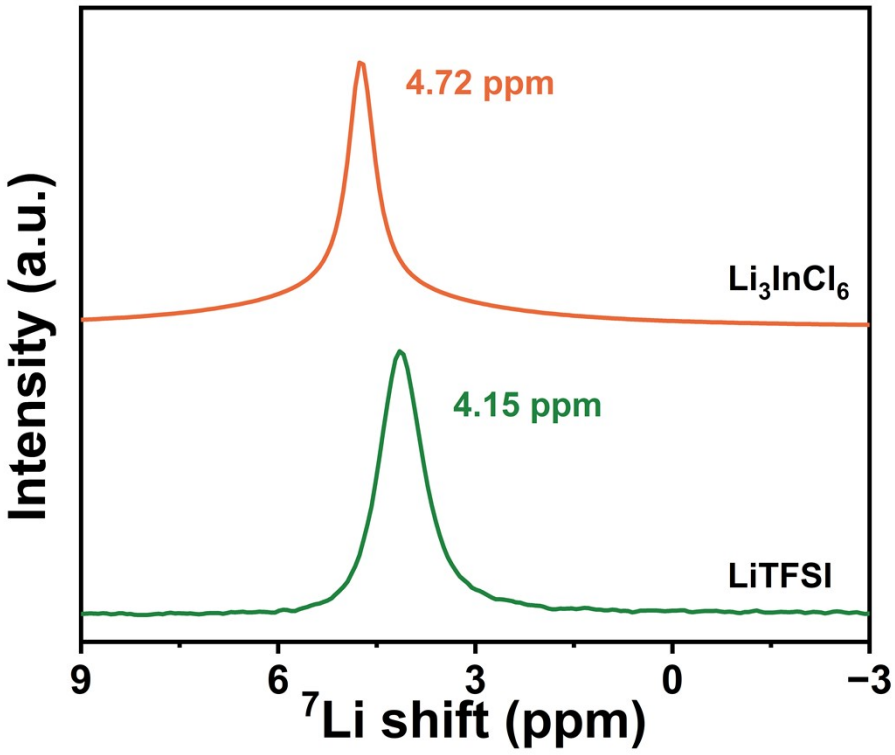

Figure S10 1D ^{7}Li MAS spectra for (a) Li_3InCl_6, (b) LiTFSI.

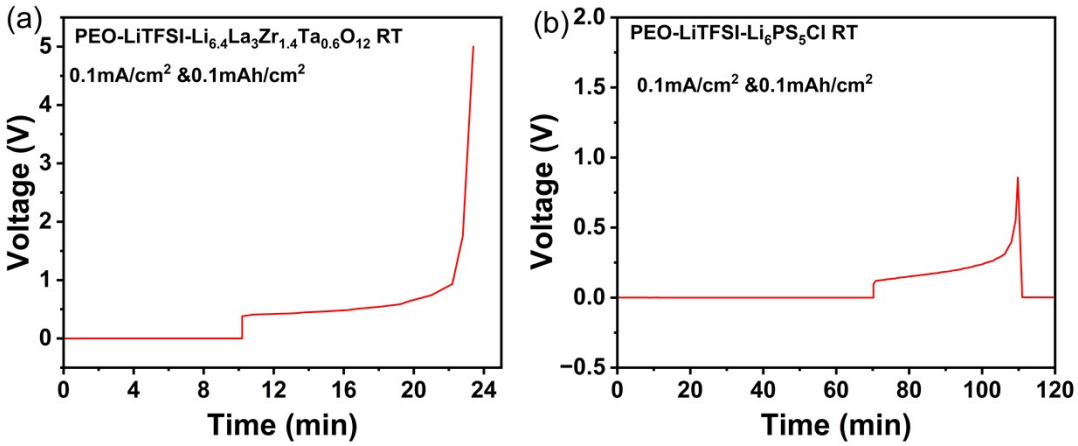

Figure S11. Galvanostatic cycling of (a) Li/LiTFSI–PEO–$Li_{6.4}La_3Zr_{1.4}Ta_{0.6}O_{12}$ CPE/Li and (b) Li/LiTFSI–PEO–Li_6PS_5Cl CPE/Li symmetric cells at room temperature under a current density of 0.1 mA cm^{-2}.

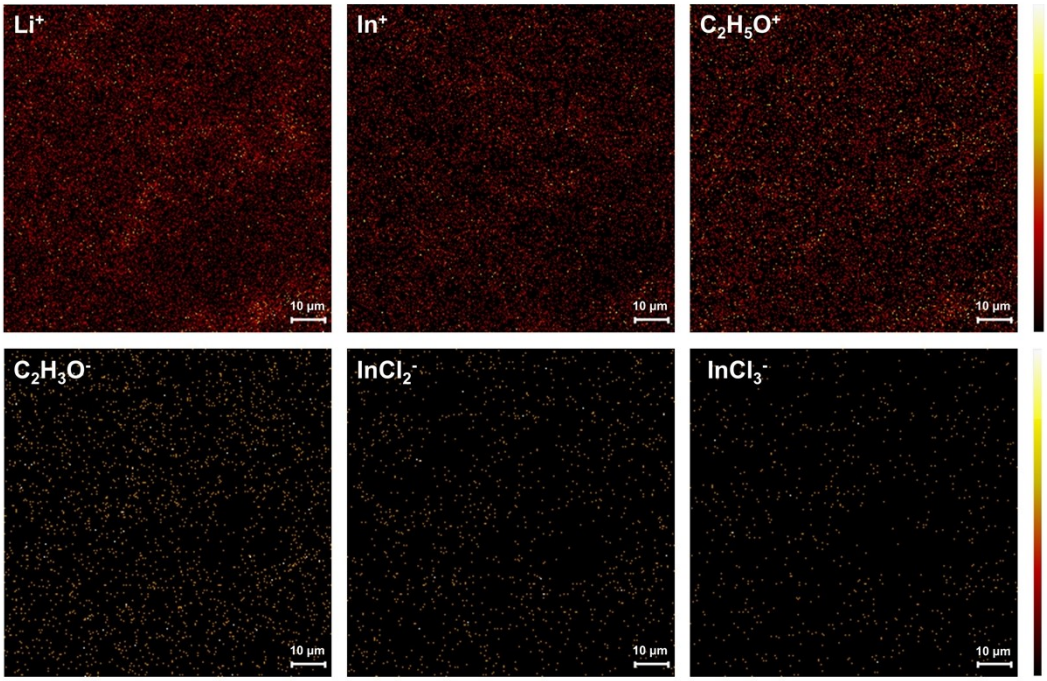

Figure S12. TOF-SIMS ion maps of the PEO–LiTFSI–Li_3InCl_6 composite electrolyte, showing the lateral distributions of Li^+, In^+, organic fragments ($C_2H_5O^+$, $C_2H_3O^+$), and indium-chloride-related species ($InCl_2^-$, $InCl_3^-$).

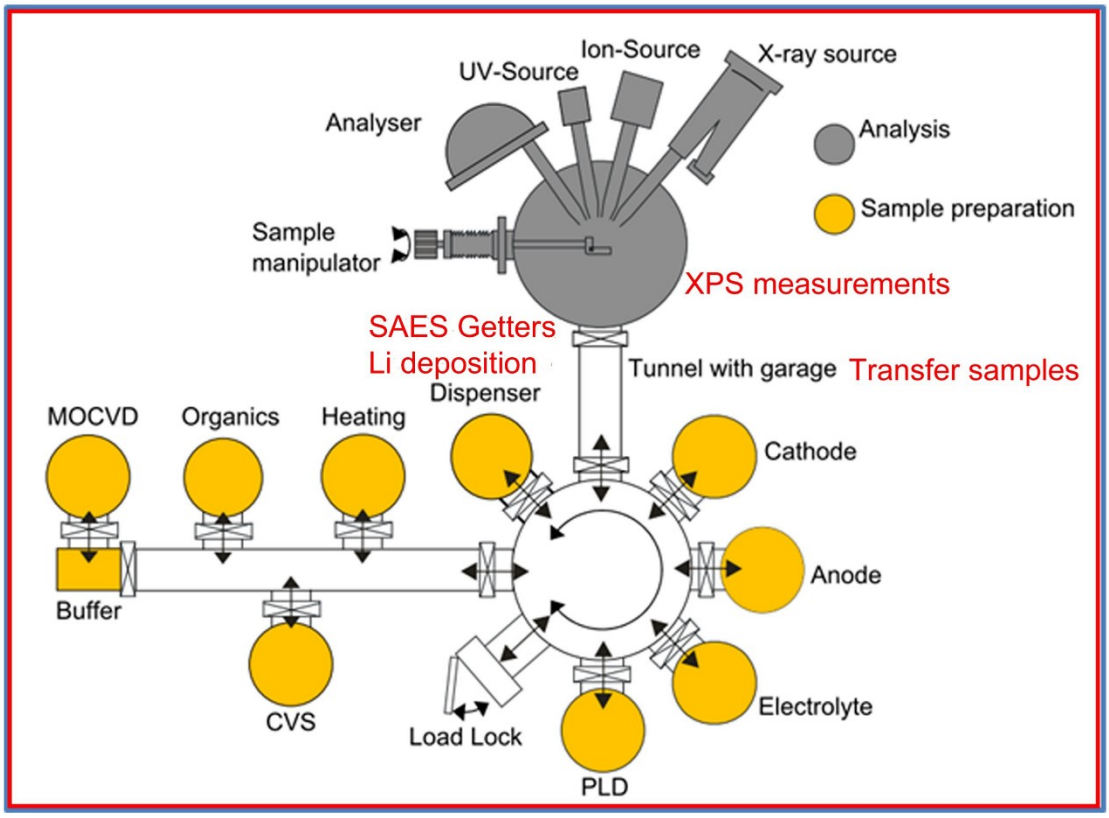

Figure S13. Scheme of the Darmstadt Integrated System for Battery (DAISY-BAT) integrated system showing the different functional chambers which are connected via an ultra-high vacuum (UHV) transfer system to the XPS/UPS analysis unit [1].

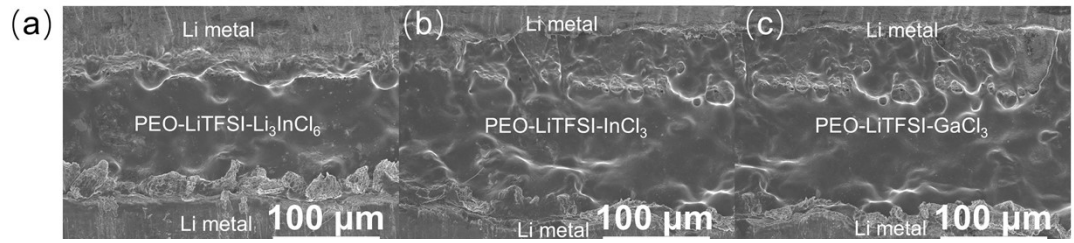

Figure S14. Cross-sectional SEM images of Li/PEO-based CPE/Li symmetric cells after cycling with different electrolytes: (a) PEO-LiTFSI-Li_3InCl_6, (b) PEO-LiTFSI-$InCl_3$, and (c) PEO-LiTFSI-$GaCl_3$, showing smooth and stable Li/electrolyte interfaces.

Table S1: R_b and R_{int} achieved from Figure S2.

	PEO-LiTFSI-Li_3InCl_6	PEO-LiTFSI	PEO-LiTFSI-$Li_{6.4}La_3Zr_{1.4}Ta_{0.6}O_{12}$
R_b	174.7 ohm cm^2	1977 ohm cm^2	2762 ohm cm^2
R_{int}	250.8 ohm cm^2	2926 ohm cm^2	4298 ohm cm^2

Table S2: R_b and R_{int} achieved from Figure S2.

	PEO-LiTFSI-$InCl_3$	PEO-LiTFSI-$GaCl_3$
R_b	266.6 ohm cm^2	237.4 ohm cm^2
R_{int}	353 ohm cm^2	583.8 ohm cm^2

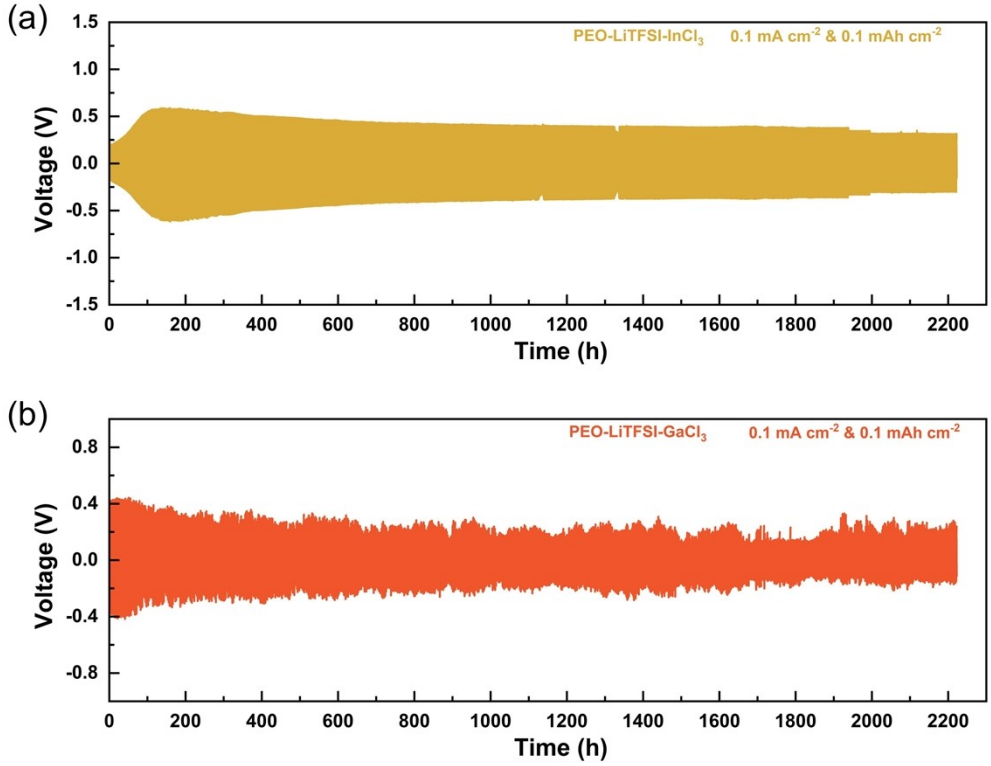

Figure S15. Long-term galvanostatic cycling of symmetric Li cells with (a) PEO-LiTFSI-$InCl_3$, and (b) PEO-LiTFSI-$GaCl_3$ electrolytes at 0.1 mA cm^{-2} and 0.1 mAh cm^{-2}.

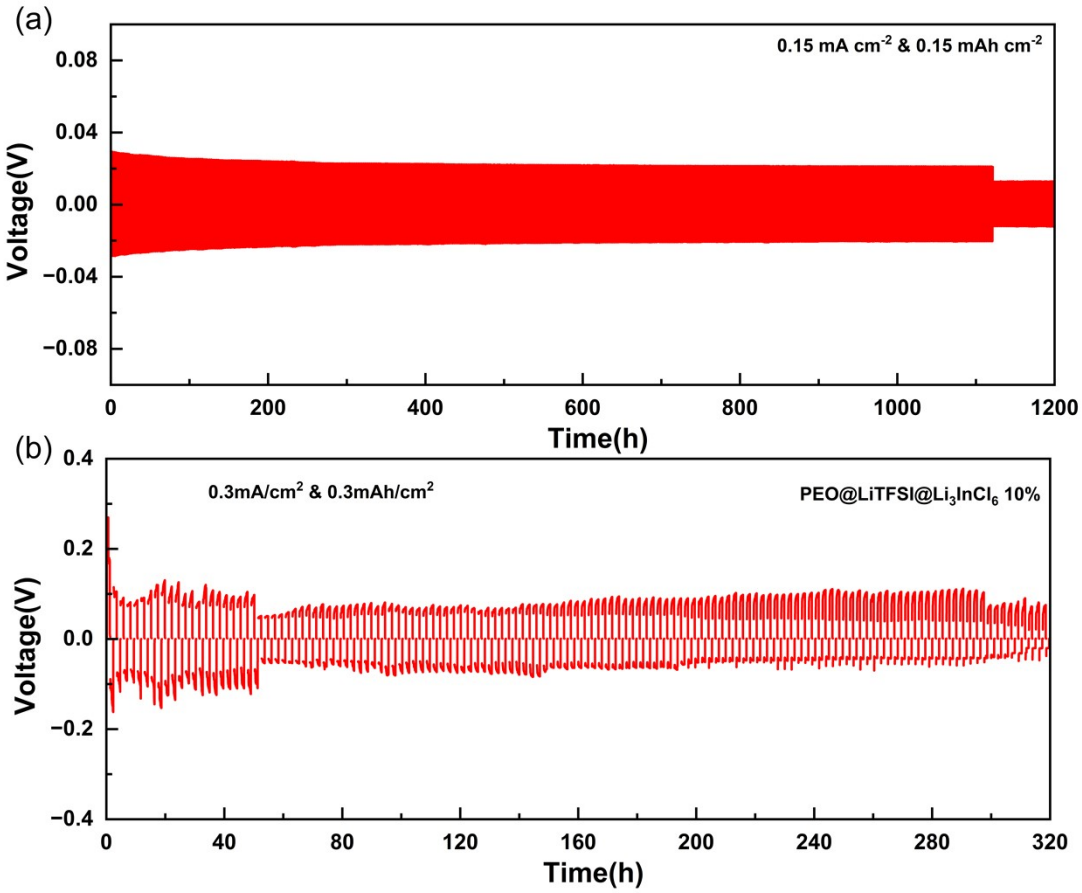

Figure S16. Galvanostatic cycling profiles of Li/LiTFSI–PEO–Li_3InCl_6 CPE/Li symmetric cells at room temperature under current densities of (a) 0.15 mA cm^{-2}, (b) 0.3 mA cm^{-2}.

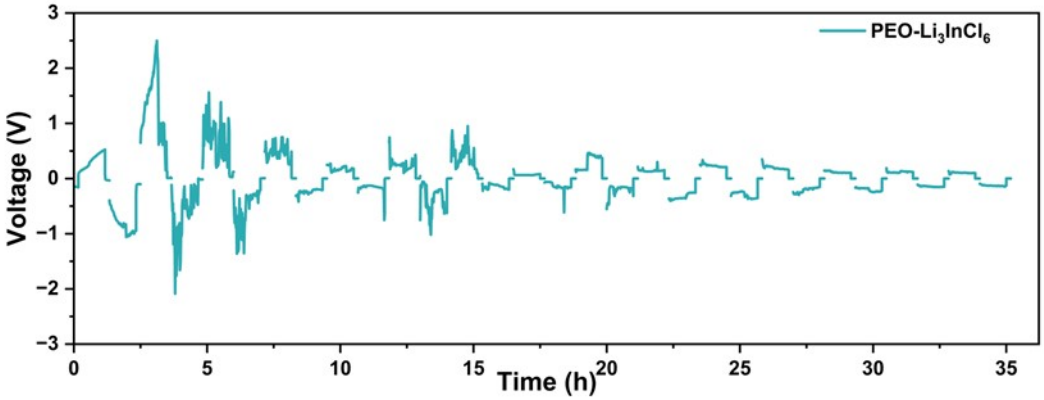

Figure S17. Galvanostatic cycling of the Li/PEO–Li_3InCl_6 CPE/Li symmetric cell at room temperature under a current density of 0.1 mA cm^{-2}.

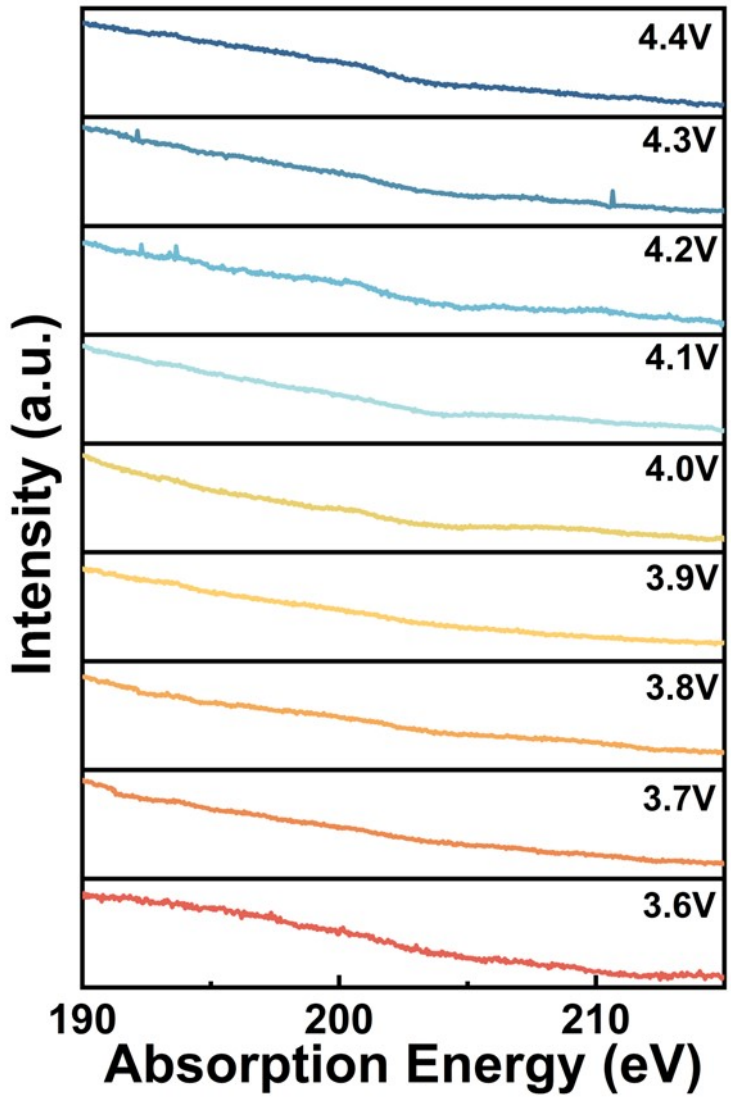

Figure S18. Normalized Cl L_3-edge XAS at different charging voltages at the NCM811/LiTFSI–PEO–Li_3InCl_6 CPE interface.

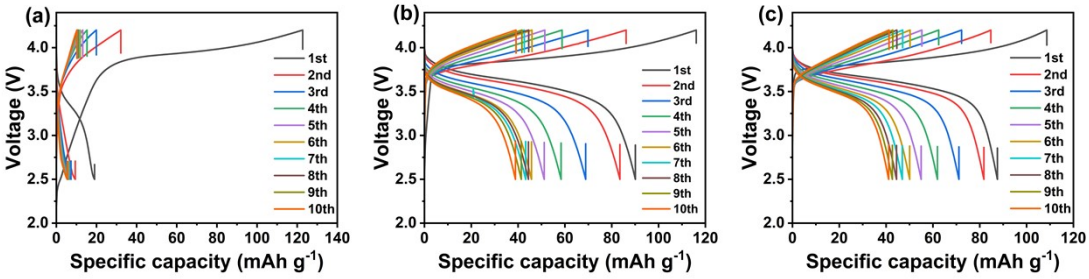

Figure S19. Charge–discharge voltage profiles of (a) NCM811/LiTFSI–PEO–Li_6PS_5Cl CPE/Li, (b) NCM811/LiTFSI–PEO CPE/Li, and (c) NCM811/LiTFSI–PEO–$Li_{6.4}La_3Zr_{1.4}Ta_{0.6}O_{12}$ CPE/Li cells at 0.1 C （19.5 A g^{-1}） and room temperature.

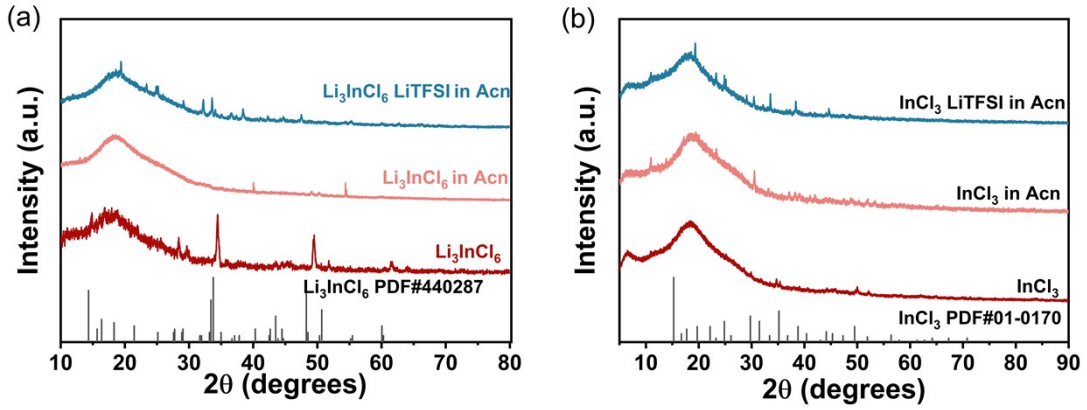

Figure S20. XRD patterns of (a) Li_3InCl_6, Li_3InCl_6 after soaking in acetonitrile, and Li_3InCl_6–LiTFSI after soaking in acetonitrile; (b) $InCl_3$, $InCl_3$ after soaking in acetonitrile and $InCl_3$–LiTFSI after soaking in acetonitrile.

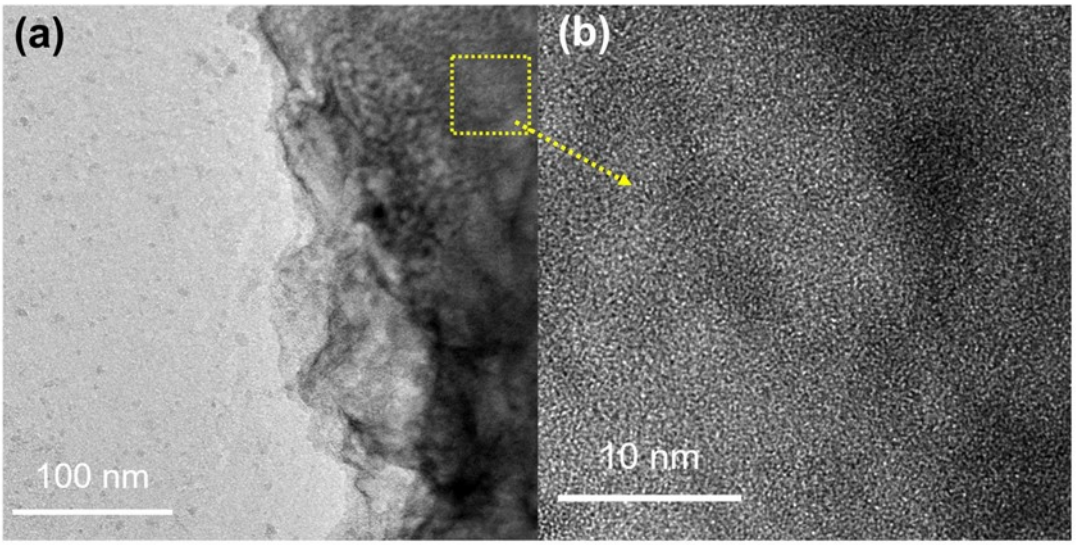

Figure S21. TEM images of Li_3InCl_6 after acetonitrile treatment. (a) Low-magnification TEM image showing a disordered, collapsed morphology without well-defined crystalline particles. (b) High-resolution TEM image exhibiting no discernible lattice fringes, confirming the loss of long-range crystalline order after acetonitrile exposure.

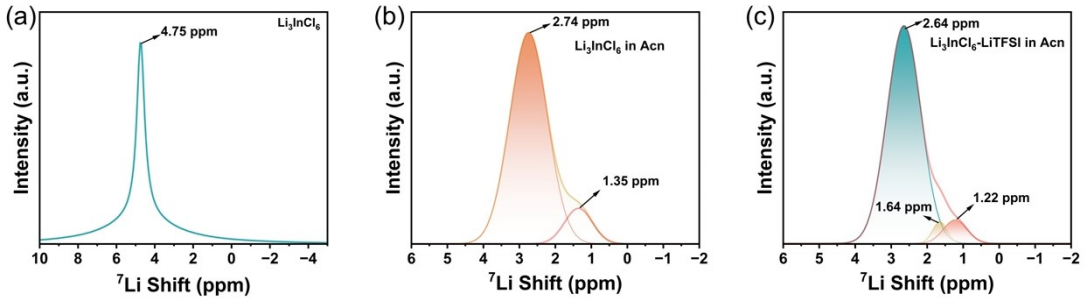

Figure S22 1D ^{7}Li MAS spectra for (a) Li_3InCl_6, (b) Li_3InCl_6 after soaking in acetonitrile and (c) LiTFSI-Li_3InCl_6 after soaking in acetonitrile.

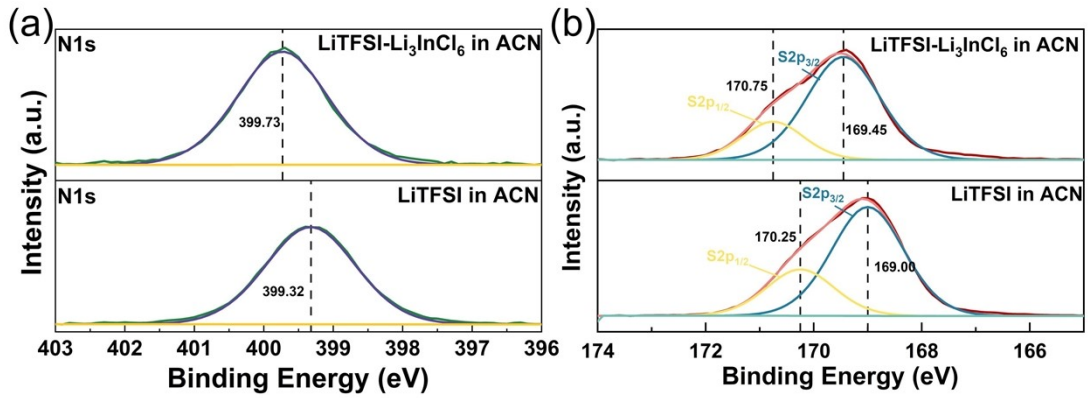

Figure S23. XPS spectra of LiTFSI and LiTFSI–Li_3InCl_6 after acetonitrile processing. (a) N 1s spectra showing a positive binding-energy shift of $TFSI^-$ in the presence of Li_3InCl_6. (b) S 2p spectra exhibiting corresponding shifts of the S $2p_{3/2}$ and S $2p_{1/2}$ components, indicating a modified coordination environment of $TFSI^-$ associated with indium-containing sites.

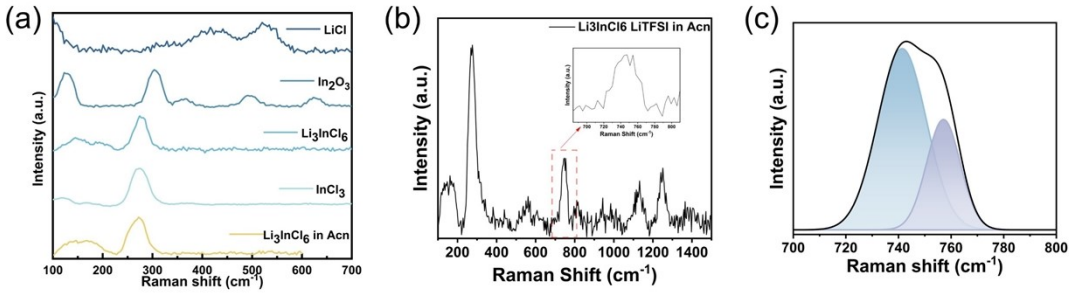

Figure S24. Raman spectra of (a) LiCl, In_2O_3, Li_3InCl_6, $InCl_3$ and Li_3InCl_6 after soaking in acetonitrile, (b) LiTFSI-Li_3InCl_6 after soaking in acetonitrile, an enlarged image of wavelengths between 700 and 800 cm^{-1} is shown in (c).

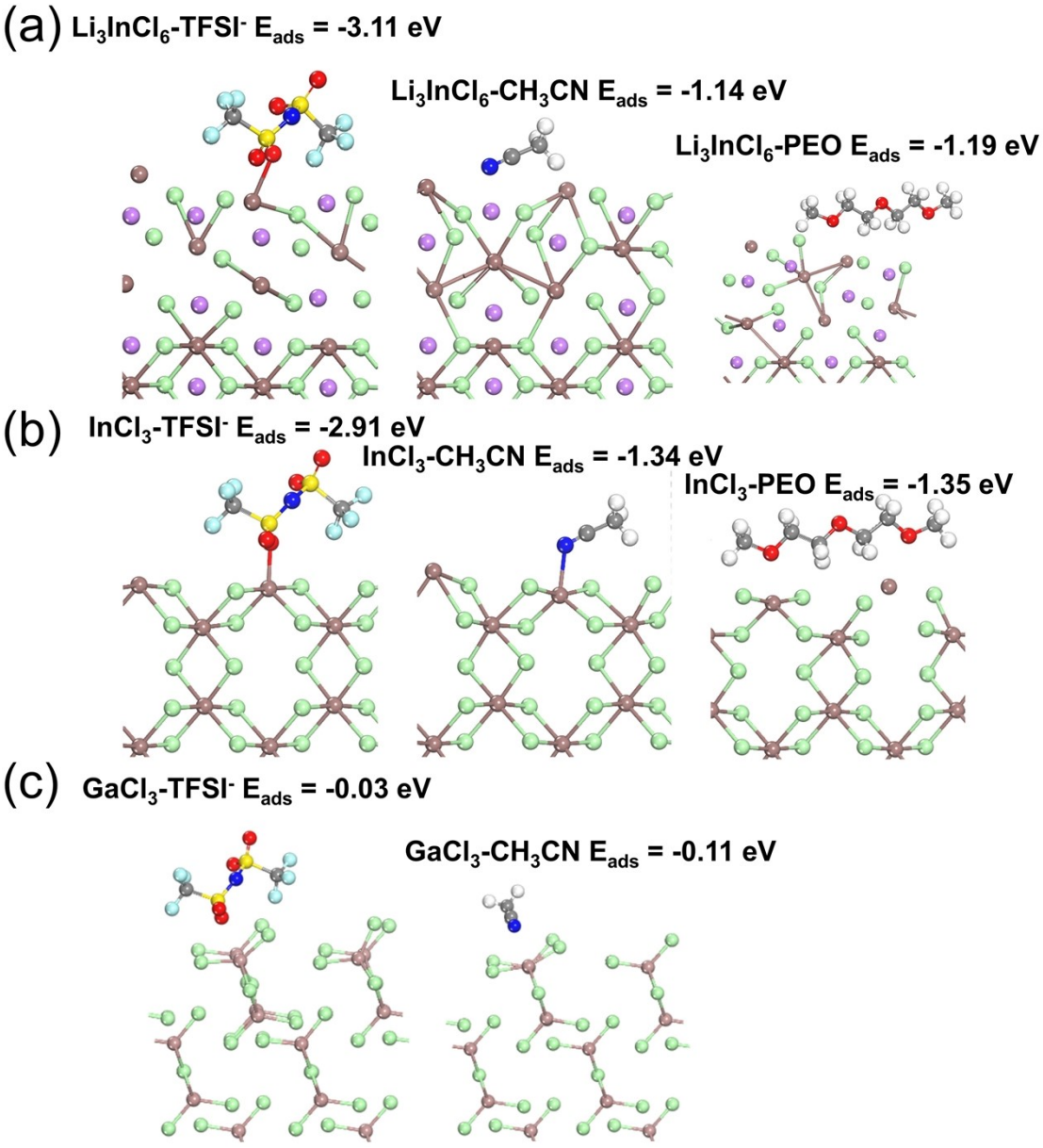

Figure S25. Simulated structures of $TFSI^-$, CH_3CN and PEO adsorbing (a) Li_3InCl_6, (b) $InCl_3$ and (c) $GaCl_3$.

Table S3. DFT results of adsorption energy.

	$TFSI^-$	CH_3CN	PEO
Li_3InCl_6	-3.31 eV	-1.14 eV	-1.19 eV
$InCl_3$	-2.91 eV	-1.34 eV	-1.35 eV
$GaCl_3$	-0.03 eV	-0.11 eV	none

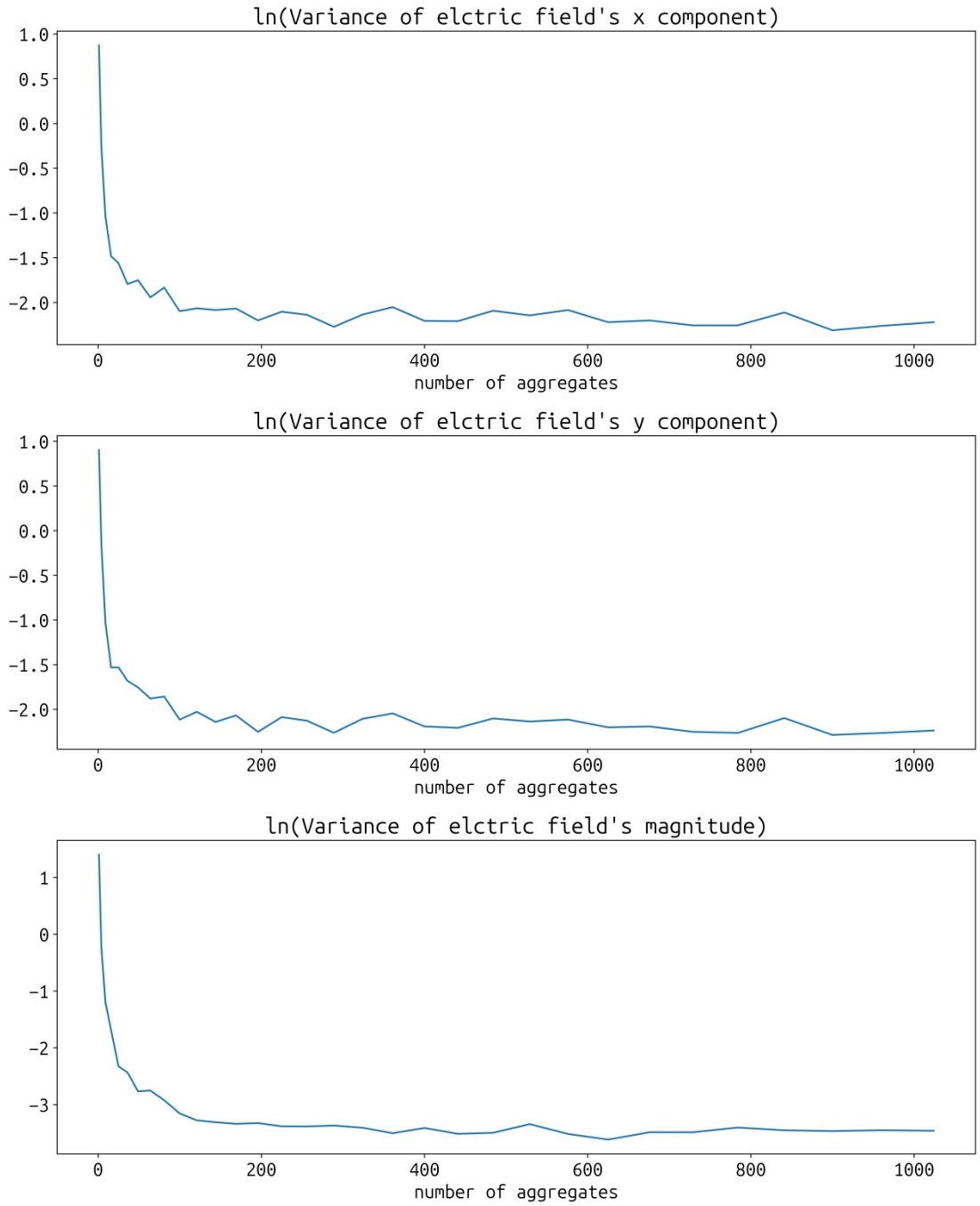

Figure S26. Variation of electric field's variance across the space (representing magnitude of local electric field) with the number of aggregates in the PEO-LiTFSI electrolyte. The vertical axis represents the logarithm of the variance. From top to bottom: x-component, y-component, and magnitude of the electric field.

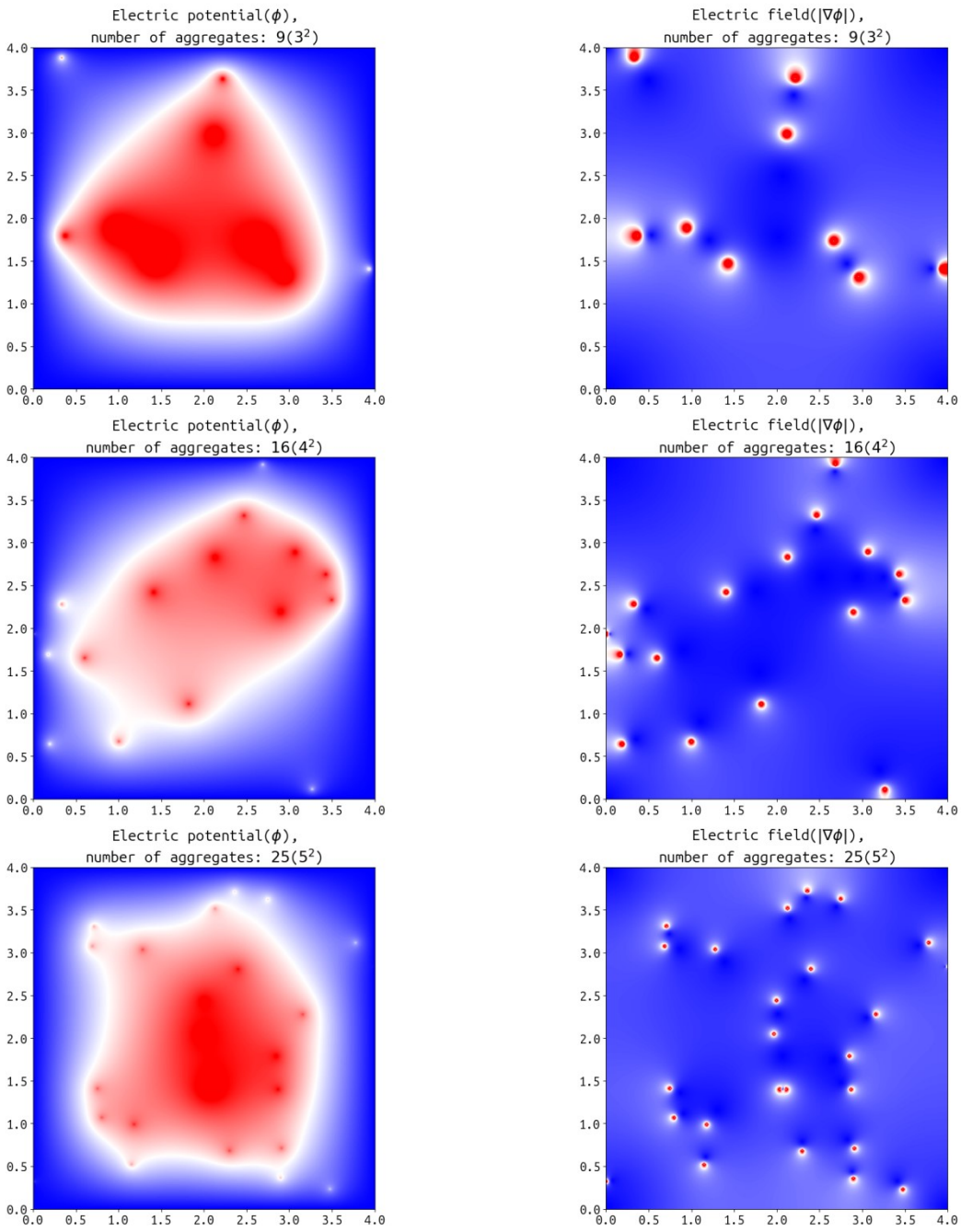

Figure S27. Contour plots of electric potential and electric field for different numbers of aggregates in the PEO-LiTFSI electrolyte. The total charge numbers of all computational areas are the same. The number of aggregates from top to bottom is 9, 16 and 25 respectively. Aggregates are randomly distributed.

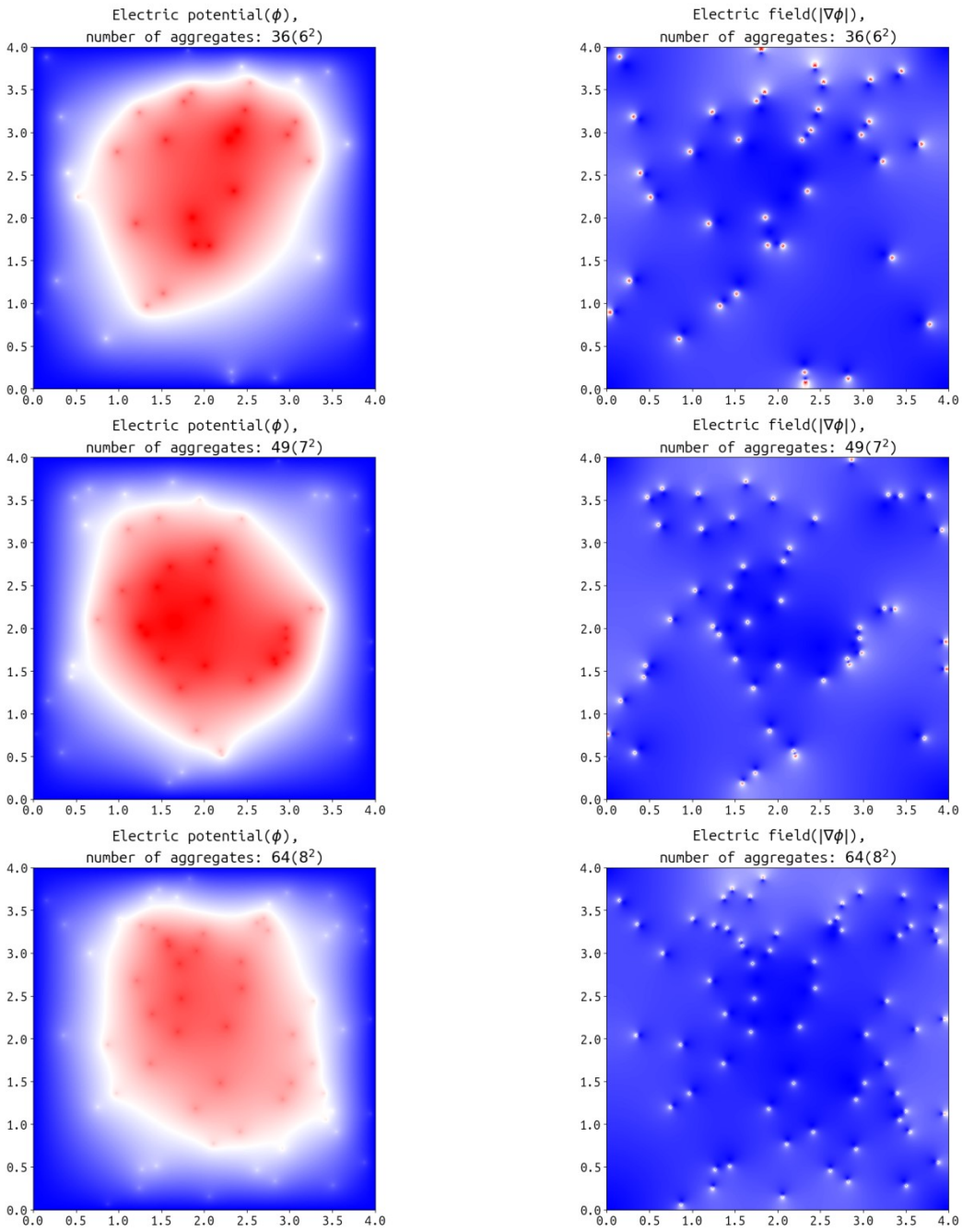

Figure S28. Contour plots of electric potential and electric field for different numbers of aggregates in the PEO-LiTFSI electrolyte. The total charge numbers of all computational areas are the same with those in Figure S9. The number of aggregates from top to bottom is 36, 49 and 64 respectively. Aggregates are randomly distributed.

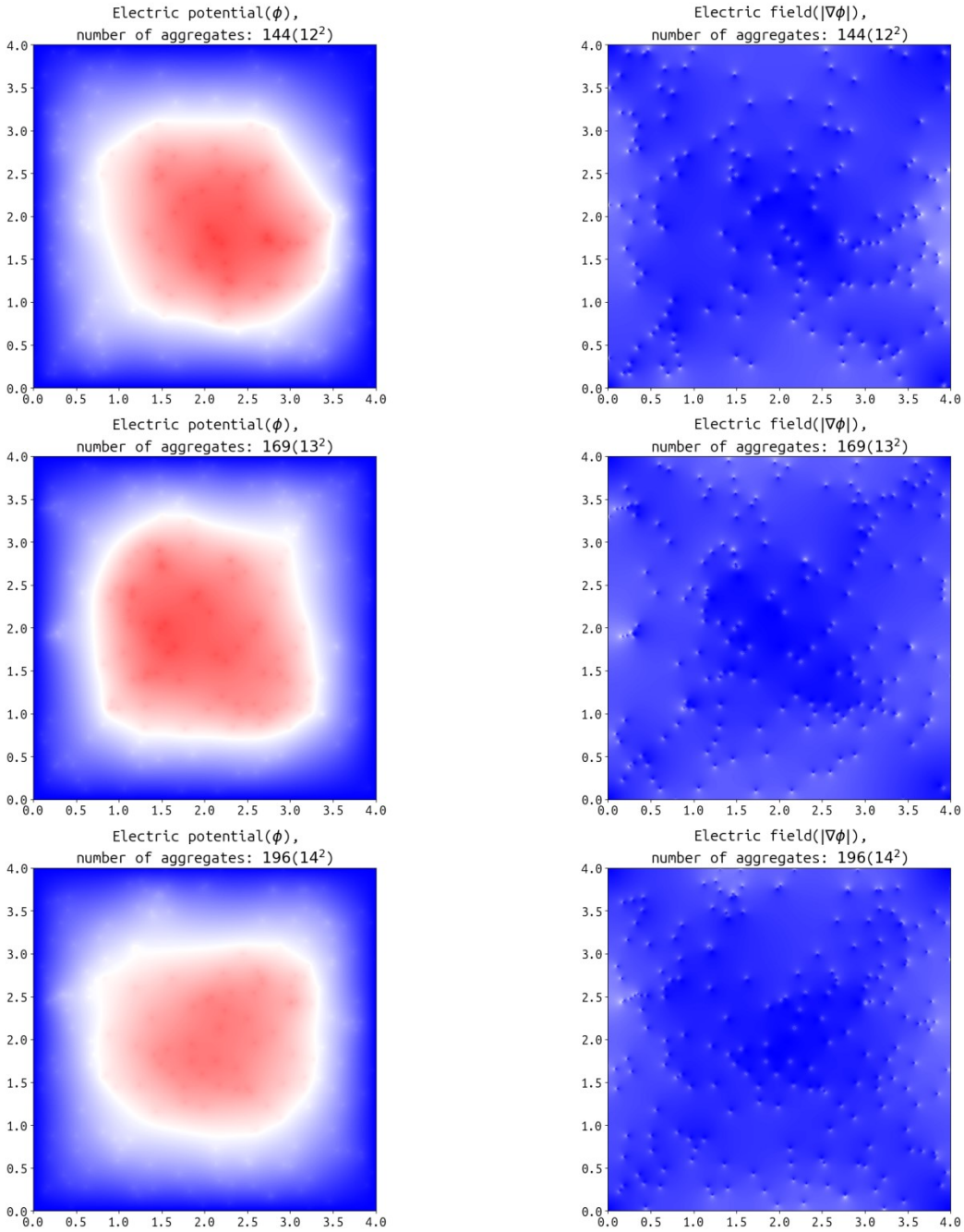

Figure S29. Contour plots of electric potential and electric field for different numbers of aggregates in the PEO-LiTFSI electrolyte. The total charge numbers of all computational areas are the same with those in Figure S27 and S28. The number of aggregates from top to bottom is 144, 169 and 196 respectively. Aggregates are randomly distributed.

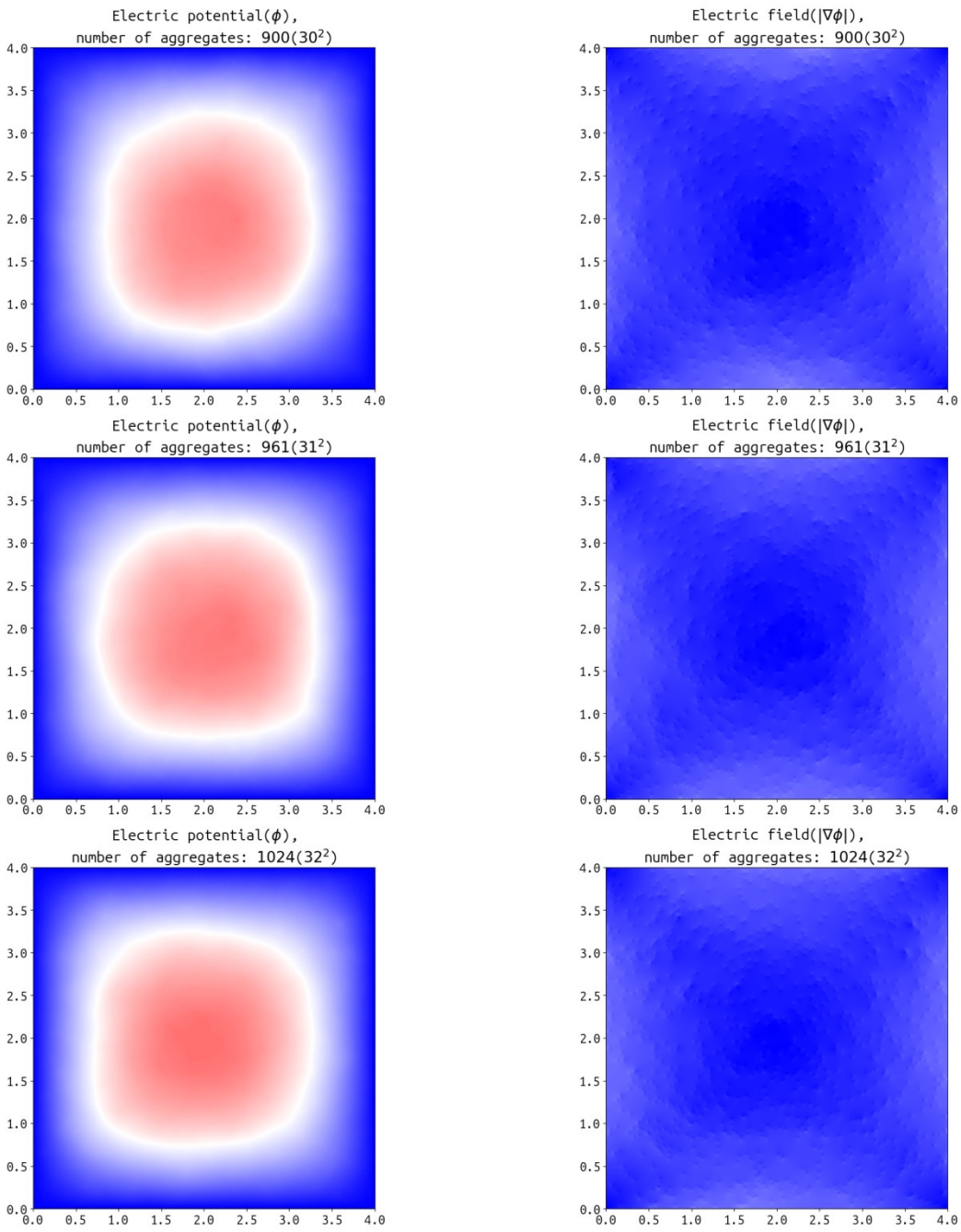

Figure S30. Computational results of electric potential and electric field for different numbers of aggregates in the PEO-LiTFSI electrolyte. The total charge numbers of all computational areas are the same as those in Figures S27-29. The number of aggregates from top to bottom is 900, 961 and 1024 respectively. Aggregates are randomly distributed.

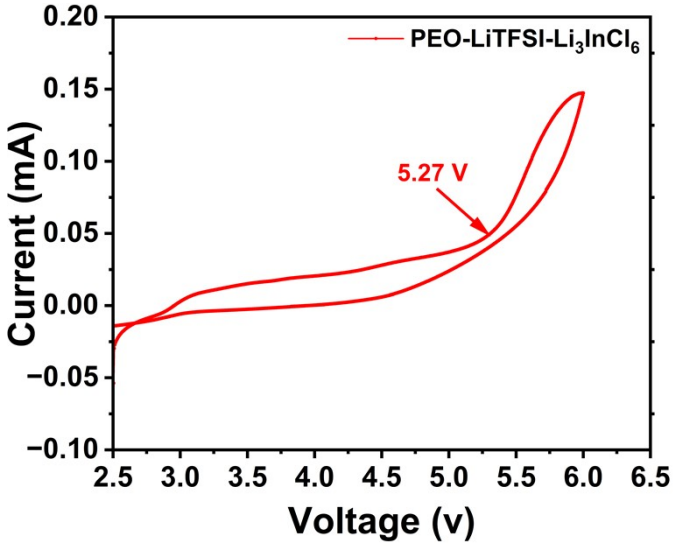

Figure S31. CV curve of the PEO–LiTFSI–Li_3InCl_6 electrolyte measured with a stainless-steel working electrode and Li reference electrode.

The CV result of the PEO–LiTFSI–Li_3InCl_6 electrolyte (Figure S31) shows that the current remains low over most of the voltage range and starts to increase noticeably at approximately 5.27 V, indicating an apparent anodic onset at this potential under the present measurement conditions. The CV measurement provides additional electrochemical evidence that is consistent with the LSV and RIXS results, supporting the conclusion that the introduction of Li_3InCl_6 enhances the oxidative stability of the electrolyte.

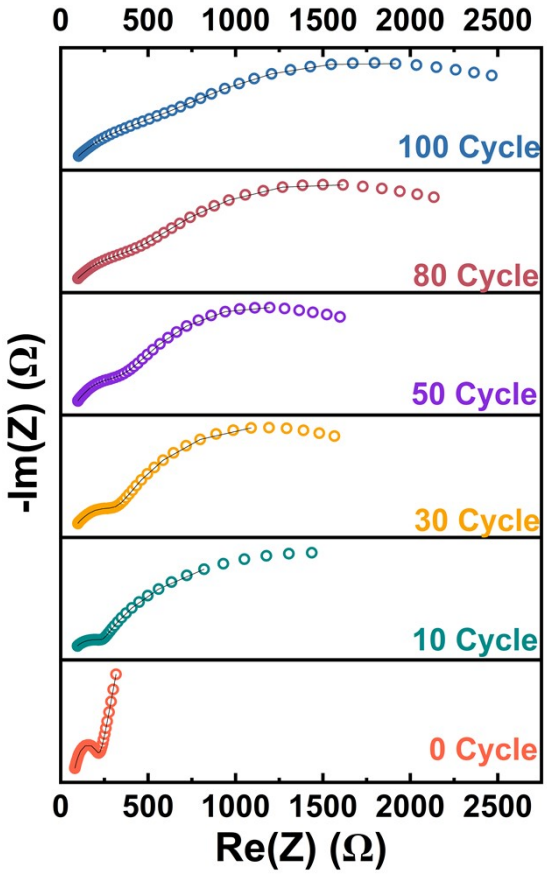

Figure S32. Nyquist plots of the NCM811/PEO–LiTFSI–Li_3InCl_6/Li cell measured at different cycling stages (0, 10, 30, 50, 80, and 100 cycles).

As is shown in figure S32, the continuous increase in impedance indicates that the electrode/electrolyte interfaces, especially the NCM811/electrolyte interface, become less favorable for charge transfer during cycling. As interfacial resistance grows, Li-ion transport across the interface becomes slower, leading to larger polarization and a lower accessible discharge capacity.

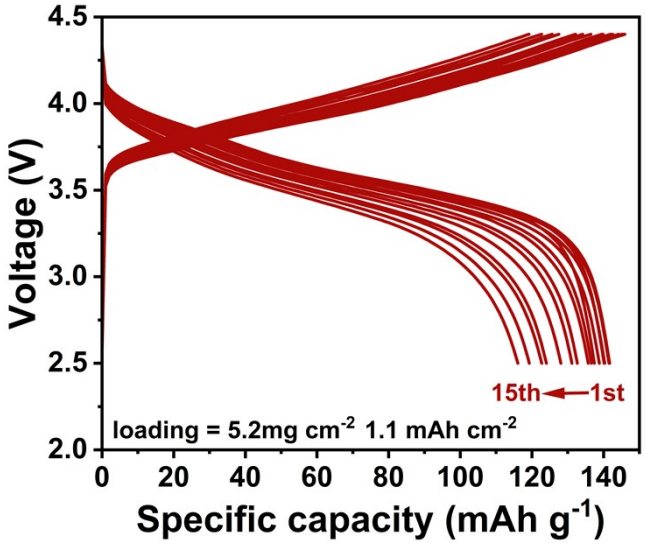

Figure S33. Charge–discharge voltage profiles of the NCM811/PEO–LiTFSI–Li_3InCl_6/Li full cell from the 1st to the 15th cycle. The cell exhibits increasing polarization and gradual capacity fading with cycling at an areal capacity of ~1.1 mAh cm^{-2}

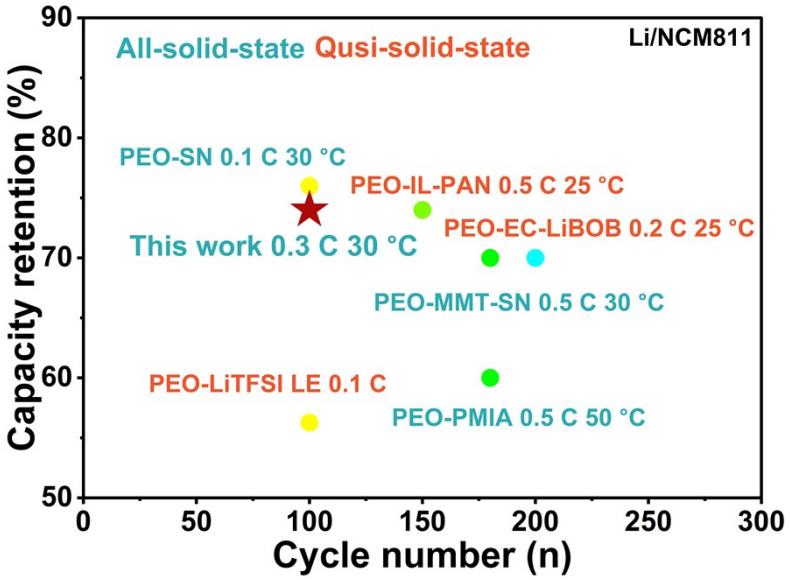

Figure S34. Comparison of cycling stability with previously reported PEO-based all-solid-state and quasi-solid-state systems, highlighting the superior performance of this work.

The performance comparison in Figure R34 highlights the cycling stability of the present work relative to previously reported PEO-based solid-state and quasi-solid-state systems.

It can be clearly observed that systems exhibiting higher capacity retention over extended cycles are predominantly either quasi-solid-state electrolytes or tested at elevated temperatures. In contrast, under room-temperature all-solid-state conditions, most reported PEO-based systems show limited cycling stability, typically with lower capacity retention or shorter cycle life.[2-8]

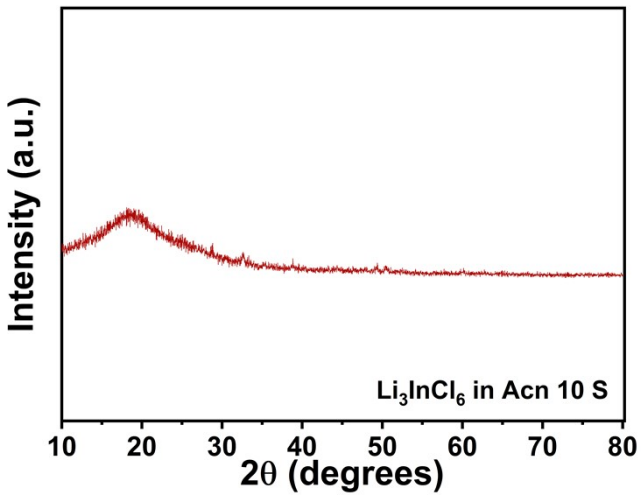

Figure S35. XRD pattern of Li_3InCl_6 after immersion in acetonitrile for ~10 s followed by rapid filtration. The disappearance of characteristic diffraction peaks indicates rapid structural collapse upon contact with acetonitrile.

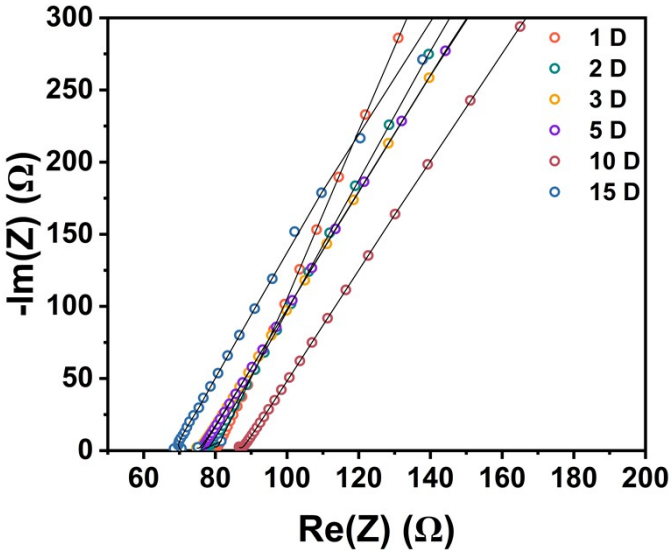

Figure S36. Nyquist plots of the stainless-steel blocking cells using PEO–LiTFSI–Li_3InCl_6 electrolytes after storage in an Ar-filled glove box for 1, 2, 3, 5, 10, and 15 days.

For the glove-box storage test, the ionic conductivity was monitored after storing the electrolyte for 1, 2, 3, 5, 10, and 15 days, as is shown in Figure S36. The impedance results show that the electrolyte maintains overall stable ion-transport characteristics during storage, without continuous monotonic deterioration over the 15-day period. Although a temporary increase in impedance is observed at 10 days, the resistance at 15 days returns to a level comparable to that of the earlier samples, indicating that the electrolyte remains reasonably stable under inert storage conditions.

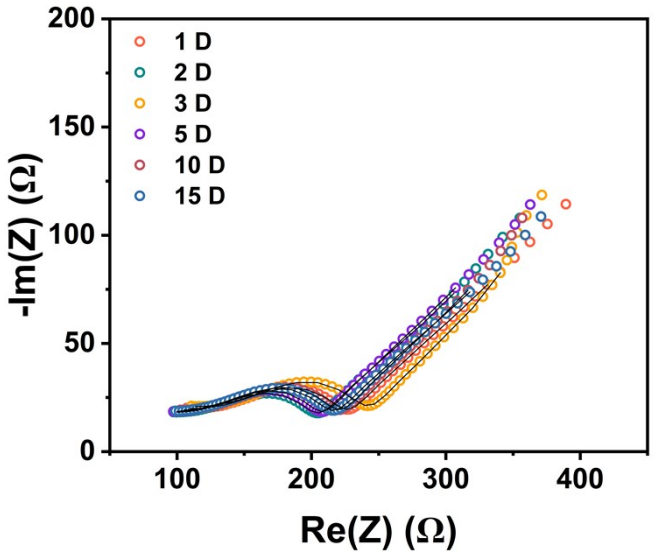

Figure S37. Nyquist plots of Li/PEO–LiTFSI–Li_3InCl_6/Li symmetric cells measured after storage for different durations in an Ar-filled glove box, showing the evolution of interfacial impedance.

EIS measurements of Li/electrolyte/Li symmetric cells (Figure S37) after storage show that the interfacial resistance remains within a comparable range during the same storage period. No abrupt or catastrophic increase in interfacial impedance is observed, suggesting acceptable interfacial stability of the electrolyte toward Li metal under glove-box storage conditions.

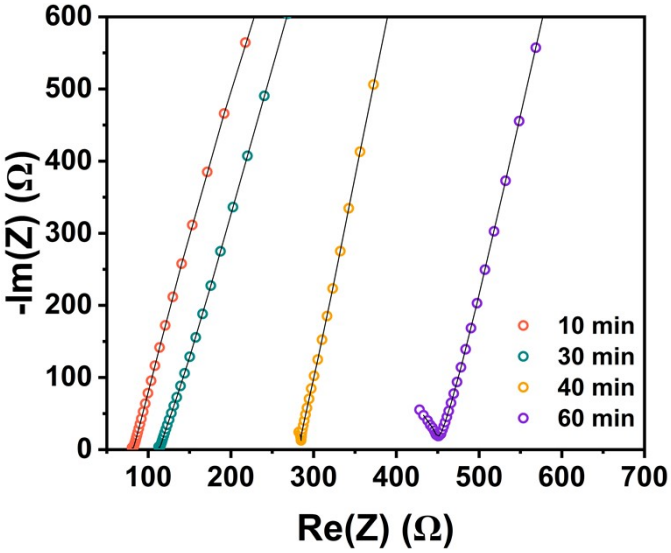

Figure S38. Nyquist plots of the electrolyte after exposure to air for 10, 30, 40, and 60 min, showing progressive impedance growth with increasing exposure time.

To evaluate environmental tolerance, the electrolyte was also exposed to air for 10, 30, 40, and 60 min before conductivity measurements (Figure S38). In this case, the impedance increases progressively with increasing air-exposure time, especially after prolonged exposure, indicating that the electrolyte exhibits only limited short-term air tolerance and undergoes significant conductivity deterioration upon longer exposure to ambient atmosphere. This result is consistent with the moisture sensitivity of halide-containing components and suggests that the electrolyte is best handled and stored under inert atmosphere.

Reference

[1]Z. Gao, J. Yang, G. Li, T. Ferber, J. Feng, Y. Li, H. Fu, W. Jaegermann, C. W. Monroe, Y. Huang, *Advanced Energy Materials* **2022**, *12*, 2103607.

[2]Z. Gao, J. Yang, G. Li, T. Ferber, J. Feng, Y. Li, H. Fu, W. Jaegermann, C. W. Monroe, Y. Huang, *Advanced Energy Materials* **2022**, *12*.

[3]M. Zuo, Z. Bi, X. Guo, *Chemical Engineering Journal* **2023**, *463*, 142463.

[4]W. Wang, Y. Yang, J. Zhang, *Nano Letters* **2025**, *25*, 3867–3874.

[5]S. H.-S. Cheng, C. Liu, F. Zhu, L. Zhao, R. Fan, C.-Y. Chung, J. Tang, X. Zeng, Y.-B. He, *Nano Energy* **2021**, *80*, 105562.

[6]M. Ye, J. Chen, H. Deng, L. Zhang, Z. Zhang, C. Zhu, M. Xiao, T. Chen, F. Wan, X. Guo, *Chemical Engineering Journal* **2024**, *488*, 151108.

[7]X.-L. Zhang, F.-Y. Shen, X. Long, S. Zheng, Z. Ruan, Y.-P. Cai, X.-J. Hong, Q. Zheng, *Energy Storage Materials* **2022**, *52*, 201–209.

[8]S. Luo, N. Deng, H. Wang, Q. Zeng, Y. Li, W. Kang, B. Cheng, *Chemical Engineering Journal* **2023**, *474*, 145683.